Chapter 1

Introduction

DEVELOPING AN UNDERSTANDING of turbulent transport in tokamaks has been a primary goal of magnetic confinement fusion research for decades. The main goal of this thesis is to develop techniques for making quantitative predictions of tokamak turbulence. These predictions can then be compared with present experiments, and used to aid in the design of future fusion reactors. While much progress has been made in both the theory of microinstabilities and experimental measurements of turbulent fluctuations in tokamaks, quantitative comparisons between experiment and non-empirical theories have been unsatisfactory in the past. This thesis presents new toroidal gyrofluid equations and nonlinear simulations which provide perhaps the most promising direct comparisons between first principles theory and experiment to date, both in levels of transport and fluctuation spectra, for actual tokamak parameters. Several advances are presented in this thesis which have been ignored in previous simulations and make these comparisons favorable, primarily: the inclusion of destabilizing toroidal effects ignored in slab theories, the use of an efficient flux tube simulation geometry for three dimensional high resolution nonlinear simulations in realistic tokamak geometry, the self-consistent evolution of small-scale turbulence generated sheared flows and realistic damping of these flows, and the inclusion of nonadiabatic electron dynamics with a sophisticated trapped electron fluid model.

1.1 Motivation

In all tokamak experiments, the particle and heat losses greatly exceed the neoclassical predictions which result from collisional diffusion. However, fluctuation measurements in tokamaks invariably see small scale (compared to the size of the tokamak, but large compared to the Debye length, λ_D) and low frequency (compared to the plasma frequency, ω_{pe}) fluctuations which apparently enhance transport above collisional levels. These fluctuations are believed to arise from microinstabilities primarily driven by the temperature and density gradients inherent in any confinement device. The fastest growing microinstabilities typically have perpendicular scales on the order of the ion gyroradius, $k_\perp \rho_i \sim 1/2$, where the ion gyroradius, $\rho_i = v_{ti}/\Omega_i$, and frequency and growth rate scales on the order of the diamagnetic drift frequency, $\omega_* = k_\theta \rho_i v_{ti}/L_n$. Here $v_{ti}^2 = T_i/m_i$ is the ion thermal velocity and $L_n = -(d \ln n_0/dr)^{-1}$ is the equilibrium density scale length. Based on mixing length estimates, the simplest description of the nonlinear saturation of these instabilities, these fluctuations should lead to particle diffusivities, D, and heat diffusivities, χ, which scale as

$$D, \chi \sim \frac{\Delta x^2}{\Delta t} \sim \frac{\gamma}{k_\perp^2} \sim \frac{1}{k_\perp \rho_i} \frac{\rho_i^2 v_{ti}}{L_n}.$$

Assuming that the dominant fluctuation scale is set by the fastest growing modes ($k_\perp \rho_i \sim 1$) yields the "gyro-Bohm" diffusivity, $D_{\mathrm{gB}} \sim \rho_i^2 v_{ti}/L_n$. While this leads to reasonable estimates for global energy confinement times [Perkins, 1990], it has several problems. The most striking disagreement is in the variation of fluctuation levels and diffusivities with minor radius. Experiments show that χ and fluctuation levels increase with increasing minor radius, while the gyro-Bohm χ decreases, because of the $T^{3/2}$ dependence. The gyro-Bohm χ is thus too high in the core, and too low at the edge, see [Horton *et al.*, 1992]. Additionally, using γ and $k_\perp$ from the fastest growing mode usually predicts diffusivities less than those measured in experiments. Another problem is that the experimentally measured fluctuation spectra peak at $k_\perp \rho_i \approx 0.1 - 0.2$ [Fonck *et al.*, 1993], not at the fastest growing wavelengths. The mixing length formula above shows that the largest eddies (smallest $k_\perp$) are the most dangerous and cause the most transport. This emphasizes the need to understand where the fluctuation spectrum peaks, i.e. why the dominant scale is at $k_\perp \rho_i \sim 0.1 - 0.2$, and not at the fastest growing scales or the longest possible scales, $k_\perp \rho_i \sim \rho_i/a \sim 0.003$. Many versions of this mixing length estimate have been proposed which compensate for the long wavelength peak in the spectrum, for example, using the maximum $\gamma/k_\perp^2$ rather than γ and $k_\perp$ for the fastest growing mode. An understanding of the nonlinear dynamics at a level beyond the simplest mixing length estimates is clearly needed, and nonlinear simulations can help sort out these various possible scaling relations.

Theoretical predictions of turbulent transport beyond this simple estimate are quite challenging. The evolution of the turbulence is intrinsically nonlinear and three dimensional. In addition, microinstabilities are strongly influenced by kinetic (velocity space) effects, since present day tokamak plasmas are in the long mean free path regime. Future experiments and reactor grade plasmas will also be in this regime. Either velocity space effects must be accurately modeled in fluid equations, or a kinetic approach which resolves velocity space is necessary, making the problem five dimensional. Our approach has been to develop simplified fluid equations which retain accurate models of the important physics for tokamak transport; primarily, long mean free path effects leading to Landau damping and its inverse, from both parallel free streaming and toroidal ∇B and curvature drifts. These reduced equations allow the use of high resolution, three dimensional, nonlinear computer simulations to investigate the turbulent dynamics in realistic tokamak geometry without further approximation. Most previous theories of tokamak turbulence have necessarily used either simplified dynamics, simplified geometry, or simplified nonlinear analysis: mixing length or quasilinear estimates, weak turbulence theory, or lower resolution computer simulations.

The combination of more accurate fluid models and fully nonlinear three dimensional simulations in toroidal geometry have resolved some of the aforementioned discrepancies between theory and experiment. In the simulations presented here, the peak in the fluctuation spectrum is at longer wavelengths than the fastest growing wavelengths (also seen in full torus gyrokinetic particle simulations [Parker *et al.*, 1993]). These toroidal gyrofluid simulations find much higher transport levels than the simplest mixing length estimates or sheared slab simulations, and bring the predictions up to the measured levels. Finally, part of the discrepancy in the radial dependence of χ is remedied by our toroidal gyrofluid equations, which give more accurate linear growth rates than have previous fluid theories. If the instabilities are nearly stable in the core and strongly unstable in the edge, or if some dependence on local parameters causes nonlinear saturation levels to increase near the edge, the radial variation of predicted and measured transport is in much better agreement. Recent comparisons between experiment and a transport model based on simulations with our toroidal gyrofluid code and linear fully kinetic calculations indicate that this is the case in the core ($r/a < 0.85$) of L-mode type discharges [DORLAND *et al.*, 1994b; KOTSCHENREUTHER *et al.*, 1994a]. Direct comparisons of the nonlinear toroidal simulations developed here with a TFTR L-mode discharge, presented in Chapter 6, show reasonable agreement, which encourages us to continue adding more physics to this code to try to explain a wider range of experimental conditions.

1.2 Brief Historical Review

The host of different of plasma instabilities can make a first foray into the microinstability literature quite daunting. An important guide to understanding this zoo is that all microinstabilities which may be considered relevant for tokamak turbulence are accurately described by the nonlinear electromagnetic toroidal gyrokinetic equation [FRIEMAN and CHEN, 1982] (with an appropriate collision operator) for all plasma species: ions, impurities, beams, and electrons (though the drift kinetic equation can be used for the electrons since the electron gyroradius is small). The wide range of instabilities in the literature arises from making assumptions that simplify this fundamental equation: each simplification generally isolates an instability, and it is given a new name. Even linearly, the complexity of the gyrokinetic equation makes it difficult to solve, and full solutions are only available numerically [REWOLDT *et al.*, 1987; KOTSCHENREUTHER *et al.*, 1994b]. Before proceeding chronologically, it is useful to have the basic results from these comprehensive numerical solutions in mind. These kinetic calculations show that for realistic tokamak parameters (low β and low collisionality) the dominant instability is either the toroidal Ion Temperature Gradient (ITG) driven instability (also called the η_i mode) or the Trapped Electron Mode (TEM), and that either the toroidal ITG mode or the TEM is linearly unstable or nearly unstable for measured tokamak parameters. Some of the distinction between the ITG and TEM is artificial, since ion and trapped electron dynamics affect both modes. The distinction arises because the toroidal ITG mode is primarily driven by the ion temperature gradient and the TEM is primarily driven by the trapped electron toroidal precession resonance. At higher β, kinetic versions of ideal MHD ballooning modes can be driven unstable [Rewoldt *et al.*, 1987], but tokamaks usually operate below this β limit, and electromagnetic corrections to the basic electrostatic instabilities are usually small. The toroidal ITG and TEM are thus the most promising candidates for explaining anomalous transport in tokamaks, and have been the focus of much work in this area. Variations of these instabilities are the most likely cause of the observed density and temperature fluctuations in large tokamak experiments, with the possible exception of the extreme edge.

Some of the major simplifications which have been used in the past are local vs. nonlocal treatment, simplified magnetic geometry, and fluid vs. kinetic treatment. In the local approximation, each Fourier harmonic of the perturbations is assumed to be independent, while physical inhomogeneities may couple these harmonics. Nonlocal treatment takes this coupling into account, and turns the local algebraic dispersion relation (zero-dimensional) into a one- or two-dimensional differential or integral equation in space. The nonlocal eigenmode is then a superposition of many coupled Fourier harmonics. The simplest magnetic geometry is an unsheared slab where B is straight and constant. The next level of complication is a sheared slab, where B is still constant, but the field lines twist. This couples the radial and parallel directions (k_r and $k_\parallel$) and makes the linear problem spatially one dimensional. In more realistic toroidal geometry where B also varies with major radius, toroidal ∇B and curvature drifts become an important destabilization mechanism, both through fluid-like and kinetic effects. In addition, the poloidal variation of the ∇B and curvature drifts introduce coupling of different poloidal harmonics (k_θ's), making the problem two dimensional. Fully nonlocal investigations in toroidal geometry awaited the development of the ballooning representation [Connor *et al.*, 1979], which reduces the problem back to one dimension by exploiting the perpendicular scale separation between the equilibrium and the fluctuations. Finally, to avoid the additional complexity of resolving velocity space, many earlier works were based on fluid equations which did not capture the kinetic effects of phase mixing and wave-particle resonances. Kinetic effects are often important for microinstabilities, and accurate stability calculations based on fluid equations require models of these effects.

The ITG mode can be isolated from the TEM by assuming that the electrons are adiabatic, which removes the trapped electron drive. The earliest investigations of the ITG instability were in simplified magnetic geometry, first in an unsheared slab [Rudakov and Sagdeev, 1961] and later in a sheared slab [Coppi *et al.*, 1967]. The magnetic shear and T_i/T_e dependence of the threshold for instability was fully treated by [Hahm and Tang, 1989] in the small ion gyroradius limit, including kinetic effects. In an unsheared or sheared slab, the ITG mode is basically an ion acoustic wave driven unstable by the ion temperature gradient. Later investigations revealed that in more realistic toroidal geometry the ITG mode can be strongly destabilized by ∇B and curvature drifts, and becomes the interchange-like toroidal ITG mode [Horton *et al.*, 1981; Coppi and Pegoraro, 1977]. The toroidal ITG mode is unstable if $\eta_i > \eta_i^{\rm crit}$, where $\eta_i = L_{ni}/L_{Ti}$. In these early oversimplified fluid limits $\eta_i^{\rm crit} \approx -1$ [Horton *et al.*, 1981], although $\eta_i^{\rm crit}$ also depends on $k_\perp^2\rho_i^2$ and $\epsilon_n = L_{ni}/R$. Later work began including the kinetic effects of parallel and toroidal drift resonances, usually keeping either parallel or toroidal drifts, but not both. [Guzdar *et al.*, 1983] retained the parallel resonance in a nonlocal treatment, while [Terry *et al.*, 1982; Biglari *et al.*, 1989; Romanelli, 1989] retained the toroidal resonance in the local limit. Both of these approaches show that the kinetic $\eta_i^{\rm crit} \approx 1$, demonstrating the importance of kinetic effects on the toroidal ITG mode. In the flat density limit where $\epsilon_n \to \infty$, the stability criterion actually becomes a criterion on L_{ti}/R instead of η_i [Tang *et al.*, 1986], and $L_{ti}/R < L_{ti}^{\rm crit}/R$ for instability. In the purely toroidal local kinetic limit (ignoring $k_\parallel$ and parallel Landau damping), [Biglari *et al.*, 1989; Dominguez and Rosenbluth, 1989] find $L_{ti}^{\rm crit}/R \approx 0.35$. The fully toroidal nonlocal kinetic calculations by [Dong *et al.*, 1992] are very complete within the context of adiabatic electrons and ignoring trapped ion effects. These results clearly demonstrate inadequacies in the local approximation. For example, in the local approximation the safety factor, q, and magnetic shear parameter, $\hat{s} = (r/q)\partial q/\partial r$, do not enter (although a q dependence can be introduced by assuming $k_\parallel = 1/qR$ in local calculations). Fig. 7 of [Dong *et al.*, 1992] shows a strong dependence of the toroidal ITG growth rate on $\hat{s}$, an effect which is completely missed within the local approximation.

Impurities and beams can also affect the toroidal ITG mode. If the impurity density is outwardly peaked (inverted), impurities can be strongly destabilizing, as was first shown in an unsheared slab by [Coppi *et al.*, 1966]. Later nonlocal investigations in sheared slab geometry [Tang *et al.*, 1980] confirmed that inverted impurity density profiles can be strongly destabilizing, and that inwardly peaked impurity density profiles are strongly stabilizing. That these trends persist in toroidal geometry was shown in the fully toroidal kinetic calculations of [Dong *et al.*, 1994]. Thus the radial variation of Z_{eff} is potentially an important stability parameter, and if Z_{eff} is peaked near the edge, this impurity destabilization may increase theoretical transport predictions in the edge, bringing them into closer agreement with experiment, as pointed out by [Dorland *et al.*, 1994a]. The effects of impurities (strongly stabilizing with flat Z_{eff}) and beam ions (weakly stabilizing) have also been demonstrated in comprehensive toroidal kinetic calculations of the toroidal ITG mode [Kotschenreuther *et al.*, 1993], and the effects of a non-Maxwellian beam distribution have been investigated by [Rewoldt and Tang, 1990] for both the toroidal ITG mode and TEM.

Another complication is the effect of trapped ions. When the mode time scales fall below the ion bounce frequency $\omega_{bi} = \sqrt{\epsilon} v_{ti}/qR$, trapped ion effects become destabilizing. Since the toroidal ITG mode typically has $\omega \sim k_\theta \rho_i v_{ti}/R$, trapped ion effects are important for long wavelengths, $k_\theta \rho_i \ll \sqrt{\epsilon}/q$. Although the trapped-ion mode and toroidal ITG mode are often considered distinct, the toroidal ITG mode gradually evolves into the trapped ion mode at long wavelengths. The work of [Xu and Rosenbluth, 1991] includes trapped ions, but assumes adiabatic electrons.

For more complete instability calculations, the adiabatic electron assumption must be relaxed. The dominant contribution to the nonadiabatic electron response comes from the bounce averaged trapped electron response; the passing electrons and non-bounce-averaged trapped electron response are usually weak [Rewoldt and Tang, 1990]. The early work on electron driven instabilities usually isolated the effects of electrons by either assuming cold ions, which considerably simplifies the analysis but removes the ITG mode, or by using a fluid ion approximation. The TEM was first investigated in the local approximation, with fluid ions and kinetic trapped electrons, with [Adam *et al.*, 1976] and without [Liu *et al.*, 1976] electron toroidal precession drifts. The nonlocal calculation with fluid ions, neglecting ion toroidal drifts, was performed by [Catto and Tsang, 1978]. A nonlocal calculation using the ballooning representation including ion toroidal drifts, for small $k_\perp \rho_i$

was presented in [CHENG and CHEN, 1981]. There is a somewhat artificial distinction between the dissipative (DTEM) and collisionless (CTEM) trapped electron modes, since the transition between them is smooth, and they are slightly different versions of the same instability.

The "ubiquitous mode" of [COPPI and REWOLDT, 1974; COPPI and PEGORARO, 1977] is the short wavelength ($k_\perp \rho_i \gtrsim 1$) version of the instabilities considered above.

In toroidal geometry, when full kinetic ions and electrons are both considered, whether the toroidal ITG mode or TEM will dominate is primarily a function of the parameters η_i, $\eta_e = L_{ne}/L_{Te}$, ϵ_n, and electron collisionality, ν_{*e}. When $\eta_i > \eta_i^{\rm crit}$ (or $L_{ti}/R < L_{ti}^{\rm crit}/R$ in the flat density gradient limit), the toroidal ITG mode dominates, but can be further destabilized by the trapped electron precession resonance. Below the ITG threshold, the TEM can still exist if ν_{*e} is sufficiently small. Because electron temperature gradients can destabilize the trapped electron mode, whether or not the TEM will be unstable below $\eta_i^{\rm crit}$ depends on η_e and ϵ_n. If the electron collisionality is large enough, the TEM drive is removed, and the plasma can be completely stable for $\eta_i \lesssim 1$.

The nonlinear saturation of these instabilities and the resulting transport is of great interest and has been considered by many authors. Because of the difficulty of nonlinear analysis, much of this work has been based on simplified fluid models and sheared slab geometry, and has focused on the ITG mode, beginning with the early fluid simulations by [HORTON *et al.*, 1980]. In an analytic fluid theory, [LEE and DIAMOND, 1986] calculated the transport expected from ITG turbulence in a sheared slab, at a much greater level of detail than mixing length estimates. Later, [TERRY *et al.*, 1988] argued that higher radial eigenmodes strongly increase the predicted slab ITG ion heat transport, suggesting that ion temperature profiles would remain close to marginality. These analytic theories required a number of uncertain assumptions and approximations. The three dimensional direct simulations of [HAMAGUCHI and HORTON, 1990] resolved a number of these uncertainties and lead to a more reasonable scaling with shear and $(\eta_i - \eta_i^{\rm crit})$. However, as a fluid model, it still neglected some important kinetic effects. The importance of kinetic effects on microinstabilities stimulated the development of gyrokinetic particle simulations [LEE, 1983; DUBIN *et al.*, 1983; LEE, 1987], used to investigate the sheared slab ITG mode in [Lee and Tang, 1988]. The sheared slab gyrokinetic particle simulations by [Kotschenreuther *et al.*, 1991] showed that fluid simulations without kinetic effects overestimate the ITG driven transport by a factor of ten. Recent work has focused on including kinetic effects in improved fluid equations by using closure approximations which model Landau damping [Hammett and Perkins, 1990] and FLR effects. These slab gyrofluid simulations [Dorland, 1993] find reduced transport compared to previous fluid simulations, bringing them into agreement with gyrokinetic particle simulations [Parker *et al.*, 1994].

These improved slab ITG gyrofluid simulations [Dorland *et al.*, 1992; Dorland, 1993] also revealed that turbulence-generated sheared flows play an important role in the development and saturation of ITG turbulence, an effect which had previously been investigated as a mechanism for the H-mode transition [Diamond and Kim, 1991; Biglari *et al.*, 1990]. This effect had also been seen in simulations of resistive drift waves [Hasegawa and Wakatani, 1987] and resistive pressure gradient driven turbulence [Carreras *et al.*, 1991], which tended to emphasize the edge. Both slab and toroidal [Beer *et al.*, 1992; Hammett *et al.*, 1993] gyrofluid simulations showed that this is also an important effect in the plasma core, and for all modes with near-adiabatic electron response. This effect had been missed in most previous ITG simulations because of limitations in the adiabatic response or in the treatment of the ($k_\theta = 0$, $k_\parallel = 0$) mode and boundary conditions. Recent gyrokinetic particle simulations have also seen this effect [Cohen *et al.*, 1993]. The importance of the generation and damping of sheared flows is even more pronounced in the toroidal ITG simulations [Beer *et al.*, 1992; Hammett *et al.*, 1993; Waltz *et al.*, 1994a] than in a sheared slab.

The obvious need to consider toroidal ITG turbulence was addressed with Braginskii-based fluid simulations first in a local 2D approximation (with $k_\parallel = 1/qR$ fixed) [Waltz, 1986], and then in full 3D toroidal geometry [Waltz, 1988]. The latter work used a rough model of Landau damping, rather than collisional based dissipation, and was one of the first in this regard. Analytic estimates of toroidal ITG transport were presented in [Biglari *et al.*, 1989]. Increasing computational power allowed full torus [Parker *et al.*, 1993] and toroidal annulus [Dimits *et al.*, 1994] gyrokinetic particle simulations. Meanwhile, the slab gyrofluid equations were extended to include the kinetic effects of toroidal drifts [Waltz *et al.*, 1992], and later improved to include more accurate models of toroidal drifts and the effects of trapped ions [Beer *et al.*, 1993]. These toroidal gyrofluid equations are simulated using a reduced flux-tube simulation geometry described in this thesis, allowing high resolution toroidal ITG simulations with kinetic effects. These simulations predict much larger transport than gyrofluid and gyrokinetic sheared slab simulations, reviving the notion that profiles may be forced to remain near marginality [Dorland *et al.*, 1994b; Kotschenreuther *et al.*, 1994a]. Recently, the trapped electron fluid equations presented in this thesis have been implemented in fully nonlinear simulations including both the trapped electron drive and the toroidal ITG drive.

A personal and readable perspective on the progress and challenges in understanding plasma turbulence through 1986 can be found in [Waltz, 1989]. A broader review through 1990 can be found in the U. S. DoE Transport Task Force Reviews on Anomalous Transport in Tokamaks in the December 1990 issue of Physics of Fluids B.

1.3 Simple Physics of the Toroidal ITG Driven Instability

Because the toroidal ITG instability is a likely cause of the observed density and temperature fluctuations in experiments, in this section the basic mechanism of the toroidal ITG instability is presented in the spirit of Cowley's picture of the slab ITG mechanism [Cowley *et al.*, 1991]. This rough picture will be based on a simple fluid model, and later chapters will introduce more physics to make our description of this instability more complete. Since later chapters will get quite complicated, it is useful to have in mind a rough picture of the structure and dynamics of these modes, and of the turbulence which ensues.

Before developing our model equations, we begin with a brief outline of the dynamics. The toroidal ITG mode is primarily driven by bad curvature effects, while the slab ITG mode is driven by parallel dynamics. Thus the toroidal version of this instability (the one most relevant to actual tokamak experiments) can be roughly described by ignoring the parallel dynamics altogether. This simplification will lead to reasonable estimates for growth rates, but cannot give the correct mode structure or the nonlinear evolution of the mode, since parallel Landau damping is the dominant damping mechanism nonlinearly. The essential difference between the slab and toroidal ITG modes is the inclusion of the toroidal ∇B and curvature drifts. For low-β equilibria, the toroidal ∇B and curvature drifts can be combined into:

$$\mathbf{v}_d = \frac{v_\parallel^2 + v_\perp^2/2}{\Omega B^2}\mathbf{B} \times \nabla B. \tag{1.1}$$

Consider a pressure perturbation with $k_r \ll k_\theta$ on the outer midplane of the tokamak as shown in Fig. 1.1. The toroidal ∇B and curvature drifts, $\mathbf{v}_d$, are down. Because of the velocity dependence of $\mathbf{v}_d$, hot particles will drift down faster than the cold particles, increasing the density below the hot spots and above the cold spots. The ion density perturbation produced by $\mathbf{v}_d$ in turn causes a potential perturbation via quasineutrality, producing the electric field as shown. This electric field induces a radial $\mathbf{E}\times\mathbf{B}$ drift, which convects hotter plasma into the hot spots and colder plasma into the cold spots, causing the perturbation to grow. On the inner midplane, where ∇p_0 is reversed but ∇B points in the same direction, this feedback mechanism is shut off. In this case the toroidal drifts produce the same density perturbation and electric field, but now $\mathbf{E} \times \mathbf{B}$ convection brings hotter plasma into the cold spots and colder plasma into the hot spots, so the perturbations are damped.

Our derivation of this instability is based on a simplified limit of the gyrokinetic equation. Setting $k_\parallel = 0$, and ignoring finite Larmor radius effects, the drift kinetic equation is (the full toroidal gyrokinetic equation is given in Eq. (2.2)):

$$\frac{\partial}{\partial t}(FB) + \nabla \cdot [FB(\mathbf{v}_E + \mathbf{v}_d)] + \frac{\partial}{\partial v_\parallel}[FBv_\parallel(\hat{\mathbf{b}} \cdot \nabla\hat{\mathbf{b}}) \cdot \mathbf{v}_E] = 0. \tag{1.2}$$

Here $\mathbf{v}_E = (c/B^2)\mathbf{B} \times \nabla\tilde{\Phi}$ is the $\mathbf{E} \times \mathbf{B}$ drift velocity, and $\tilde{\Phi}$ is the perturbed electrostatic potential. The gyrokinetic equation is written here in conservative form, and the combination FB appears because B is the Jacobian of the transformation from $(v_\parallel, v_\perp)$ to the $(v_\parallel, \mu)$ variables used here, where $\mu = v_\perp^2/2B$ is the magnetic moment adiabatic invariant. The $\partial/\partial v_\parallel$ term conserves toroidal angular momentum: an $\mathbf{E} \times \mathbf{B}$ drift which moves a particle in major radius ($\hat{\mathbf{b}} \cdot \nabla\hat{\mathbf{b}}$ is in the ∇B direction) causes a parallel acceleration.

Simplified fluid equations can be derived by taking moments of Eq. (1.2) over velocity space. For example, the particle density is:

$$n = \int d^3v F = 2\pi \int_{-\infty}^{\infty} dv_\parallel \int_0^{\infty} d\mu B F \tag{1.3}$$

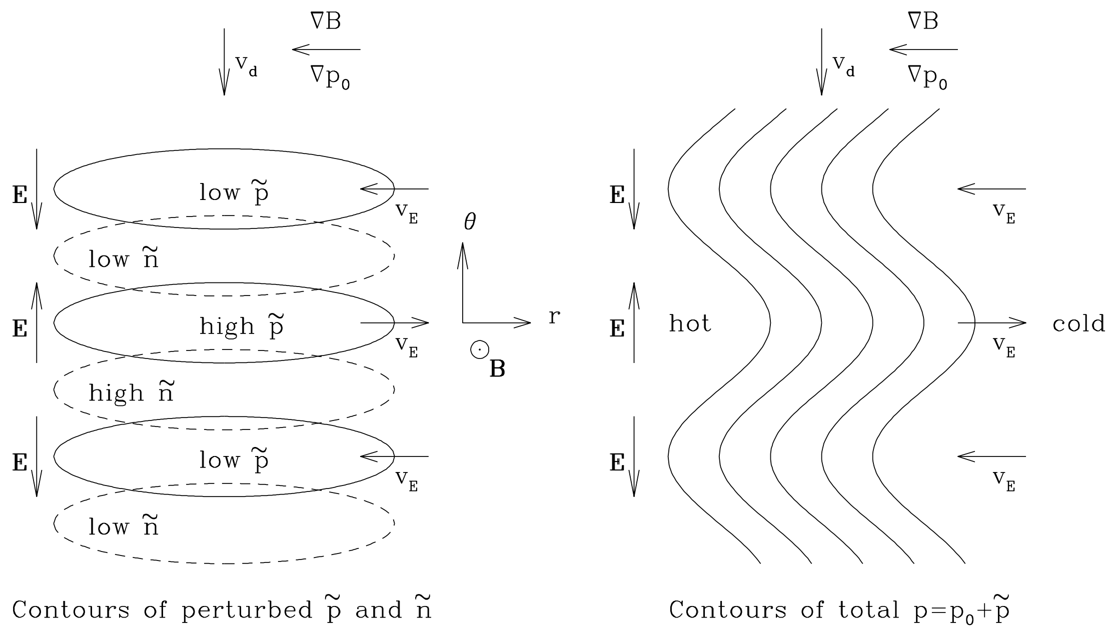

Figure 1.1: Simple picture of the toroidal ITG instability mechanism on the outer midplane of a tokamak. The velocity dependence of the downward ∇B and curvature drifts cause ion density build-up below the hot spots and above the cold spots. This produces the electric field, which $\mathbf{E} \times \mathbf{B}$ convects hotter plasma into the hot spots, and colder plasma into the cold spots. On the inner midplane where ∇p_0 is reversed with respect to ∇B, colder plasma is convected into the hot spots, and this feedback mechanism is shut off.

When taking moments of Eq. (1.2), the $v_\parallel^2$ and $v_\perp^2/2$ in $\mathbf{v}_d$ introduce the parallel and perpendicular pressures into the density equation, $p_\parallel = \int d^3v\, m v_\parallel^2 F$ and $p_\perp = \int d^3v (m v_\perp^2/2) F$. To avoid the complexity of evolving $p_\parallel$ and $p_\perp$ separately (as in Chapter 2), for the present simple model, assume that $v_\parallel^2 = v_\perp^2/2$ when taking moments of this term, i.e., the curvature drift is replaced by the ∇B drift. This is commonly called the ∇B approximation [Terry *et al.*, 1982]. The differences between the ∇B model and the constant energy resonance model, $v_\parallel^2 + v_\perp^2/2 = 2(v_\parallel^2 + v_\perp^2)/3$ [Romanelli and Briguglio, 1990], will not appear within the context of this simple fluid model. Integrating Eq. (1.2) over velocity space gives the evolution of the perturbed density:

$$\frac{\partial n}{\partial t} + \nabla \cdot \left[n\mathbf{v}_E + \frac{2p}{m\Omega B^2}\mathbf{B} \times \nabla B \right] = 0, \tag{1.4}$$

where the pressure $p = \int d^3v (mv^2)/3 = \int dv_\parallel \int d\mu B F m (v_\parallel^2 + 2\mu B)/3 \approx \int dv_\parallel \int d\mu\, B F m \mu B$ in the ∇B approximation. Breaking the density into equilibrium and perturbed parts, $n = n_0 + \tilde{n}$:

$$\frac{\partial \tilde{n}}{\partial t} + \mathbf{v}_E \cdot \nabla n_0 + \mathbf{v}_E \cdot \nabla \tilde{n} + n_0 \nabla \cdot \mathbf{v}_E + \frac{2}{m\Omega B^2}\mathbf{B} \times \nabla B \cdot \nabla \tilde{p} = 0. \tag{1.5}$$

The second term is the $\mathbf{E} \times \mathbf{B}$ convection of the equilibrium density gradient, and the third term is the nonlinear convection of the perturbed density. In the fourth term, as shown in Chapter 2, $\nabla \cdot \mathbf{v}_E = (2c/B^3)\mathbf{B} \times \nabla B \cdot \nabla \tilde{\Phi}$. This term arises from the variation of B with major radius in a tokamak; $\nabla \cdot \mathbf{v}_E = 0$ if B is constant, as in a sheared slab model. Also discussed in Chapter 2, $\nabla \cdot [(1/\Omega B^2)\mathbf{B} \times \nabla B] \approx 0$, so it comes out of the divergence, leaving the $\mathbf{v}_d$ term above. The divergence of the $\mathbf{v}_d$ drift comes from the fact that hot particles ∇B drift faster than cold particles, as shown by Eq. (1.1), so pressure perturbations cause density perturbations. The toroidal angular momentum conserving term vanishes upon integrating over $v_\parallel$.

The notation can be simplified by normalizing perturbed quantities to their equilibrium values, $n = \tilde{n}/n_0$, $p = \tilde{p}/p_0$, $\Phi = e\tilde{\Phi}/T_{i0}$, where $p_0 = n_0 T_0$, and introducing the diamagnetic drift and toroidal drift frequencies:

$$i\omega_* = \frac{cT_{i0}}{eB^2 n_0}\mathbf{B} \times \nabla n_0 \cdot \nabla, \tag{1.6}$$

$$i\omega_d = \frac{cT_{i0}}{eB^3}\mathbf{B} \times \nabla B \cdot \nabla. \tag{1.7}$$

In the usual low aspect ratio tokamak geometry, with $B = (B_0 R_0/R)(\mathbf{e}_\phi + r/qR_0\mathbf{e}_\theta)$, these frequencies become: $\omega_* = -k_\theta \rho_i v_{ti}/L_{ni}$ and $\omega_d = -(\rho_i v_{ti}/R)(k_r \sin\theta + k_\theta \cos\theta)$. In this discussion we will only consider non-inverted profiles, so $L_{ni}^{-1} = -d\ln n_{i0}/dr$ and $L_{Ti}^{-1} = -d\ln T_{i0}/dr$ are positive. The linearized density equation is then:

$$\frac{\partial n}{\partial t} - i\omega_* \Phi + 2i\omega_d \Phi + 2i\omega_d p = 0. \tag{1.8}$$

To find the evolution equation for the pressure, multiply Eq. (1.2) by $m\mu = mv_\perp^2/2B$ and integrate over velocity to get:

$$\frac{\partial}{\partial t}\frac{p}{B} + \nabla \cdot \left[\frac{p}{B}\mathbf{v}_E + \int d^3v F \frac{mv_\perp^2}{2B}\mathbf{v}_d\right] = 0. \tag{1.9}$$

The toroidal drift terms now introduce the $v_\parallel^2 v_\perp^2$ and $v_\perp^4$ moments. The simplest way to evaluate these terms is to assume that F is Maxwellian:

$$F = \frac{n}{(2\pi/m)^{3/2} T_\perp \sqrt{T_\parallel}} e^{-mv_\parallel^2/2T_\parallel - m\mu B/T_\perp}, \tag{1.10}$$

but with total (equilibrium plus perturbed) n, $T_\parallel$, and $T_\perp$. Then

$$\int d^3v F \frac{mv_\perp^2}{2B} \frac{v_\parallel^2 + v_\perp^2/2}{\Omega B^2} \mathbf{B} \times \nabla B = \frac{p_\parallel p_\perp + 2p_\perp^2}{nm\Omega B^3} \mathbf{B} \times \nabla B. \tag{1.11}$$

This is effectively a closure approximation for the $v_\parallel^2 v_\perp^2$ and $v_\perp^4$ moments in terms of the lower known moments (n and p). Better closure approximations will be introduced in Chapter 2 which model the phase mixing associated with toroidal drifts and its related resonances.

Again separating the equilibrium and perturbed parts, and approximating $p_\parallel = p_\perp$ in Eq. (1.11), the pressure equation Eq. (1.9) becomes:

$$\frac{\partial \tilde{p}}{\partial t} + \mathbf{v}_E \cdot \nabla p_0 + \mathbf{v}_E \cdot \nabla \tilde{p} + p_0 \nabla \cdot \mathbf{v}_E + p_0 B \mathbf{v}_E \cdot \nabla \frac{1}{B} + \frac{p_0}{n_0 m \Omega B^2} \mathbf{B} \times \nabla B \cdot \nabla (6\tilde{p} - 3\tilde{n} T_0) = 0. \tag{1.12}$$

Upon normalizing and linearizing, the $\nabla \cdot \mathbf{v}_E$ and $B\mathbf{v}_E \cdot \nabla(1/B)$ terms combine to give $3i\omega_d\Phi$, and the $\mathbf{v}_E \cdot \nabla p_0$ term becomes $-i(1+\eta_i)\omega_*\Phi$ using $\eta_i = L_{ni}/L_{Ti}$. The pressure equation is then:

$$\frac{\partial p}{\partial t} - i(1+\eta_i)\omega_* \Phi + 3i\omega_d \Phi + i\omega_d(6p - 3n) = 0. \tag{1.13}$$

For normal modes, the pressure and density are given by:

$$n = -\frac{\omega_*}{\omega}\Phi + 2\frac{\omega_d}{\omega}\Phi + 2\frac{\omega_d}{\omega}p, \tag{1.14}$$

$$p = \frac{-\omega_*(1+\eta_i)\Phi + 3\omega_d\Phi - 3\omega_d n}{\omega - 6\omega_d}. \tag{1.15}$$

Although $k_\parallel$ has been ignored so far, in reality these modes have $k_\parallel \sim 1/qR$. Because of their fast parallel motion, the electrons are nearly adiabatic ($k_\parallel v_{te} \sim v_{te}/qR \gg \omega \sim \omega_*$), and the perturbed electron density is given by $\tilde{n}_e/n_{e0} = e\tilde{\Phi}/T_{e0}$. Nonadiabatic electron response, which primarily comes from trapped electrons, can significantly affect these modes in some regimes, and will be considered in Chapter 3. The perturbed densities are quasineutral, since $k\lambda_D \ll 1$. Keeping the small $b = k_\perp^2\rho_i^2$ limit of the polarization density, Eq. (2.9), the perturbed electron and ion densities are related by:

$$\tilde{n}_e = \tilde{n}_i - b\frac{e\tilde{\Phi}}{T_{i0}}n_{i0},$$

Substituting $\tilde{n}_e = n_{e0}e\tilde{\Phi}/T_{e0}$ and again normalizing to $n_{e0} = n_{i0}$, and $\Phi = e\tilde{\Phi}/T_{i0}$,

$$\frac{T_{i0}}{T_{e0}}\Phi = n - b\Phi,$$

or

$$(\tau + b)\Phi = n, \tag{1.16}$$

where $\tau = T_{i0}/T_{e0}$.

The dispersion relation for this simple model is quadratic, and is obtained by combining Eqs. (1.14), (1.15), and (1.16):

$$(\tau+b)\omega^2 + \omega[-6\omega_d(\tau+b) + \omega_* - 2\omega_d] + 6\omega_d^2(1+\tau+b) + 2\omega_*\omega_d(\eta_i - 2) = 0. \tag{1.17}$$

with roots:

$$\omega = \frac{6\omega_d(\tau+b) + 2\omega_d - \omega_*}{2(\tau+b)} \pm \frac{\sqrt{[6\omega_d(\tau+b) + 2\omega_d - \omega_*]^2 - 4(\tau+b)[6\omega_d^2(1+\tau+b) + 2\omega_d\omega_*(\eta_i-2)]}}{2(\tau+b)} \tag{1.18}$$

The growth rate from this simple model is shown in Fig. 1.2 for $\eta_i = 2$, $\tau = 1$, $b = 0$, and varying $\epsilon_n = L_n/R$. Also shown are the fully kinetic and gyrofluid growth rates

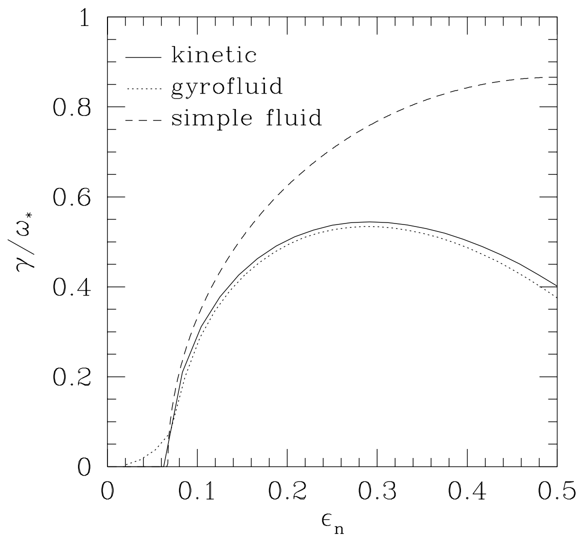

Figure 1.2: Comparison of kinetic, gyrofluid, and simple fluid growth rates of the purely toroidal ITG mode, for $\eta_i = 2$. Including models of kinetic effects significantly improves the accuracy of the gyrofluid results.

corresponding to this purely toroidal limit, as found in Chapter 2. Including kinetic effects brings the gyrofluid results into much better agreement with kinetic theory than the simple model discussed here, but this simple model captures the gross features of the instability.

In is instructive to first look at the flat density gradient limit, where $L_{ni} \to \infty$, so ϵ_n and $\eta_i \to \infty$. In this limit Eq. (1.18) reduces to:

$$\omega = \frac{3\omega_d(\tau + b) + \omega_d}{(\tau + b)} \pm \frac{\sqrt{3\omega_d^2(\tau + b)^2 + \omega_d^2 - 2\omega_d\omega_*\eta_i(\tau + b)}}{(\tau + b)} \tag{1.19}$$

To get instability, we need $2\omega_d\omega_*\eta_i(\tau + b) > 3\omega_d^2(\tau + b)^2 + \omega_d^2$. Clearly, $\omega_d\omega_*\eta_i > 0$ is necessary (but not sufficient) for instability, since the other terms inside the square root in Eq. (1.19) are positive. From this condition, it can be ascertained from the definitions of ω_* and ω_d in Eqs. (1.6) and (1.7) that ∇p_0 and ∇B must point in the same direction for instability ("bad" curvature), and if ∇p_0 and ∇B are antiparallel ("good" curvature) the mode is stable. Because $\omega_* = -k_\theta\rho_i v_{ti}/L_{ni}$ and $\omega_d = -(\rho_i v_{ti}/R)(k_r \sin\theta + k_\theta \cos\theta)$, perturbations on the outer midplane of the torus ($\theta = 0$) are unstable, while perturbations on the inner midplane ($\theta = \pi$) are stable.

The dispersion relation Eq. (1.19) shows the stabilizing effect of $T_{i0} > T_{e0}$, ($\tau > 1$), both in the threshold for instability, because the stabilizing $3\omega_d^2(\tau + b)^2$ term increases more rapidly with τ than the destabilizing $-2\omega_d \omega_* \eta_i(\tau + b)$ term, and in the growth rate, because the $(\tau + b)$ in the denominator beats the $\sqrt{\tau + b}$ coming from the drive. This stabilization of the toroidal ITG mode from $T_{i0} > T_{e0}$ is a likely mechanism for improved transport in supershots and hot-ion modes (in combination with relatively weak electron temperature gradients to keep TEM driven transport small). The stabilizing effect of $T_i > T_e$ occurs by reducing the ion density perturbation produced by Φ, weakening the feedback mechanism that causes instability, as discussed below. In addition, Eq. (1.19) shows some of the stabilizing influence of finite Larmor radius (FLR) effects through b, though the FLR corrections in the density and pressure equations have been neglected. Physically, FLR stabilization occurs because the ions feel the averaged potential around their gyro-orbits, and this gyroaveraging reduces the response to high $k_\perp \rho_i$ components of the potential. In the large η_i (strongly unstable) limit, Eq. (1.19) gives a purely growing root:

$$\omega \approx \pm i \sqrt{\frac{2\omega_d \omega_* \eta_i}{\tau + b}}. \tag{1.20}$$

Since $\omega_*, \omega_d \propto k_\perp$, the growth rate stops increasing with b near $b = k_\perp^2 \rho_i^2 = 1$. With the more complete FLR terms in Chapter 2, the growth rates peak around $k_\perp \rho_i \sim 1/2$, and then drop. Though ignored in this simple model, the perturbed impurity and beam densities can also affect stability, as discussed in the previous section.

In the slab limit, where $\epsilon_n \to 0$ so the toroidal terms vanish, the two roots of Eq. (1.18) are neutrally stable, $\omega = 0$ (the ion acoustic wave) and $-\omega_*/(\tau + b)$ (the electron drift wave). Parallel dynamics are necessary for instability in the slab limit.

To see the physical mechanism of this instability, consider a perturbation on the outer midplane in the large η_i limit, where the mode is purely growing ($\gamma \gg \omega_r$). Assuming $\tau = 1$ and neglecting FLR corrections ($b = 0$), from Eq. (1.20) we find $\gamma = \sqrt{\eta_i \omega_d \omega_*} = \sqrt{2\omega_d \omega_{*T}}$. Eqs. (1.14) and (1.15) become: $\Phi = -2\omega_d p/\omega$ and $p = -\omega_* \eta_i \Phi/\omega$. Using $\Phi = \bar{\Phi} \exp[ik_\theta r_0 \theta - i\omega t]$ and $p = \bar{p} \exp[ik_\theta r_0 \theta - i\omega t + i\alpha]$, where $\bar{\Phi}$ and $\bar{p}$ are real,

$$\Phi(\theta, t) = \Re[\Phi + \Phi^*]/2 = \bar{\Phi}\cos(k_\theta r_0 \theta)\exp(\gamma t),$$

$$p(\theta, t) = \Re[p + p^*]/2 = \bar{p}\cos(k_\theta r_0 \theta + \alpha)\exp(\gamma t).$$

From Eq. (1.15), taking $k_\theta > 0$, so $\omega_* < 0$:

$$\bar{p}e^{i\alpha} = \frac{-\eta\omega_*}{i\gamma}\bar{\Phi} \Rightarrow \alpha = -\pi/2,$$

thus the perturbed pressure will be $\pi/2$ out of phase with the potential, leading to the density perturbations as shown in Fig. 1.1, and the instability mechanism from $\mathbf{E} \times \mathbf{B}$ convection of the equilibrium pressure.

Now going back to the general dispersion relation, Eq. (1.17), but assuming $\tau = 1$ and $b = 0$, the roots are:

$$\omega = 4\omega_d - \frac{\omega_*}{2} \pm \frac{1}{2}\sqrt{16\omega_d^2 + \omega_*^2 - 8\omega_d\omega_*\eta_i}. \tag{1.21}$$

In this more general case, the $\mathbf{E} \times \mathbf{B}$ convection of n_0, and $\nabla \cdot \mathbf{v}_E$ (the first two terms on the RHS of Eq. (1.14) are not negligible (as they were in the large η_i limit), so the phase shift between the density and pressure perturbations will not be $\pi/2$. This makes the mode propagate; it propagates in the ion direction for $\epsilon_n > 1/8$ and in the electron direction for $\epsilon_n < 1/8$. For $b = 0$ and $\tau = 1$, the quasineutrality constraint, Eq. (1.16), gives $n = \Phi$, so Eq. (1.15) becomes:

$$p = \frac{-\omega_*(1 + \eta_i)}{\omega - 6\omega_d}\Phi. \tag{1.22}$$

When the phase shift between p and Φ is large enough ($\alpha = 0$ or π for $\gamma = 0$), the feedback mechanism is shut off and the mode is stabilized. For this simple model, this occurs at:

$$\eta_i^{\mathrm{crit}} = \frac{1 + 16\epsilon_n^2}{8\epsilon_n},$$

and the mode is unstable for $\eta_i > \eta_i^{\mathrm{crit}}$. This is a reasonable approximation to the kinetic η_i^{crit}, which is a also function of ϵ_n, but is always greater than 2/3. In the flat density limit, $\epsilon_n \to \infty$, $\eta_i^{\mathrm{crit}} \to 2\epsilon_n$, so the critical η_i becomes a critical temperature gradient, $L_{Tc}^{\mathrm{sf}}/R = 0.5$ from this simple fluid model, and instability requires $L_T < L_{Tc}$. The toroidal gyrofluid equations in Chapter 2 give $L_{Tc}^{\mathrm{gf}}/R = 0.33$, which is a better approximation to the kinetic $L_{Tc}^{\mathrm{kin}}/R = 0.36$.

Now consider a mode with $k_r \neq 0$, so the perturbations pictured in Fig. 1.1 are tilted in the poloidal plane. At the outer midplane, since $\sin\theta = 0$, ω_d is unchanged; also, ω_* is unchanged. The toroidal drifts still produce density perturbations aligned with the pressure perturbations, and $\mathbf{E} \times \mathbf{B}$ convection is along these tilted perturbations, leading to the same instability. Thus the only effect of k_r is to increase $b = k_\perp^2 \rho_i^2$, which is stabilizing, so $k_r = 0$ perturbations are the most unstable.

In a real tokamak these perturbations are aligned with the magnetic field lines, since parallel Landau damping or phase mixing quickly damps any high $k_\parallel$ components. As a field line rotates around the magnetic axis (from B_p), it samples both good and bad curvature regions. Minimizing $k_\parallel$ while simultaneously localizing the modes in the bad curvature region leads to mode structures with $k_\parallel \approx 1/qR$, with large amplitude at the outer midplane and smaller amplitude at the inner midplane ("ballooning" mode structure). In addition, magnetic shear causes the field lines on neighboring flux surfaces to rotate at different rates. The perturbations try to follow this twisting, which increases k_r moving along the field line. This increases FLR stabilization away from the point where $k_r = 0$. Thus the parallel mode structure is determined by the competition between minimizing $k_\parallel$, localizing the mode in the bad curvature region, and magnetic shear localization through FLR effects.

These instabilities grow until the nonlinear $\mathbf{E} \times \mathbf{B}$ terms in Eqs. (1.5) and (1.12) become comparable to the linear terms. For radially elongated modes as pictured in Fig. 1.1, $\nabla\tilde{n}$ and $\nabla\tilde{p}$ are nearly perpendicular to $\mathbf{v}_E$, so the nonlinearity is weak, allowing these modes to grow to large amplitude. However, these elongated modes may be susceptible to "secondary instabilities" [Cowley *et al.*, 1991], and are strongly affected by radially sheared perpendicular flows, which stretch and twist the perturbations, enhancing decorrelation and reducing the fluctuation amplitudes [Biglari *et al.*, 1990]. From this simple picture, we expect these modes to evolve into turbulent blobs with short perpendicular scales, $k_\perp\rho_i \lesssim 1/2$, and long parallel scales, $k_\parallel \sim 1/qR$ (i.e. very elongated along the field line), with ballooning mode structures. These gross features are in fact observed in the more complete nonlinear simulations discussed in Chapter 5.

1.4 Outline

1.4.1 Improved Toroidal Gyrofluid Equations

The inclusion of ∇B and curvature drift effects is an important destabilization mechanism for tokamak microinstabilities. The growth rates for the toroidal ITG mode are typically three to four times higher than the growth rates of the slab ITG mode. Using models similar to [Waltz *et al.*, 1992], toroidal gyrofluid equations with more accurate closure approximations to model toroidal phase mixing are derived in Chapter 2. These toroidal gyrofluid equations also incorporate models of parallel phase mixing [Hammett and Perkins, 1990] and linear and nonlinear FLR effects [Dorland and Hammett, 1993], although the linear FLR terms are slightly modified by toroidicity. The derivation presented in Chapter 2 is valid for finite $k_\parallel$, while [Waltz *et al.*, 1992] focused on the purely toroidal ($k_\parallel = 0$) limit and a term to remove a singularity for finite $k_\parallel$ was added *a posteriori*.

Slab [Dorland *et al.*, 1992; Dorland, 1993] and toroidal [Beer *et al.*, 1992; Hammett *et al.*, 1993] simulations revealed that an important nonlinear saturation process for tokamak turbulence is the nonlinear generation and damping of radially sheared "zonal" $\mathbf{E} \times \mathbf{B}$ flows (flows which cause flux surfaces to rotate). These sheared flows are very weakly damped in a sheared slab (via classical viscosity); the dominant damping mechanisms arise from toroidal effects. The mirroring $\mu\hat{\mathbf{b}} \cdot \nabla B$ term is included in these toroidal gyrofluid equations to provide accurate models of poloidal flow damping from magnetic pumping, and also to model the effects of trapped ions, which extend the validity of these equations into the trapped ion regime at low $k_\theta \rho_i$. Finally, a Krook collision operator has been incorporated, important for poloidal flow damping in the Pfirsch-Schlüter regime, and for collisional effects on very low frequency modes.

1.4.2 Fluid Models for Trapped Electrons

Trapped electron models developed in this thesis have provided the first high resolution three dimensional toroidal simulations which simultaneously include trapped-electron effects as well as the ITG drive, which we presented in [Hammett *et al.*, 1994]. This enables realistic nonlinear calculations of the full transport matrix (electron and ion heat fluxes and particle fluxes). Previous ITG simulations using adiabatic electrons had no electron heat flux or particle flux. A sophisticated trapped electron fluid model is derived in Chapter 3 which retains the pitch angle dependence throughout, as opposed to more simplified trapped electron models which assume that the electrons are deeply trapped [Kadomtsev and Pogutse, 1970]. Retaining this pitch angle dependence is potentially important for advanced tokamak configurations in the second stability regime or with reversed magnetic shear [Kessel *et al.*, 1994], where a major fraction of the trapped electrons have favorable toroidal precession drift, stabilizing trapped electron modes. Because these electron equations are bounce averaged, the fast parallel electron time scale is removed, and nonlinear simulations with trapped electrons are only about two times slower than simulations assuming adiabatic electrons. We can now study regimes where the collisionless or dissipative trapped electron mode (TEM) dominates over the ITG mode, or in mixed regimes where the TEM drive may double the growth rate of the ITG mode. These simulations can also investigate why the core of supershots are convection dominated, or search for "off-diagonal" pinch effects.

1.4.3 Flux Tube Simulation Geometry

Simulation of turbulence in a full tokamak is very challenging since one must simultaneously resolve the machine size and the scales of the turbulence. The scale of the turbulence is on the order of the ion gyroradius, ρ_i, while the size of present day tokamaks is much larger, $a/\rho_i \sim 500 - 1000$, where a is the minor radius. This requires a very fine computational grid, and is slightly beyond today's computational capabilities for realistic a/ρ_i. In Chapter 4 a reduced simulation geometry is presented which resolves only a thin flux tube rather than the full torus, exploiting the elongated nature of the turbulence, which has short perpendicular scales but long parallel scales. This method allows high resolution simulations in realistic tokamak geometry, retaining the important toroidal effects of good and bad curvature. It is also applicable to non-tokamak magnetic configurations, and the formulation in Chapter 4 is presented in a form applicable to general magnetic geometry. The material in Chapter 4 is available as a PPPL report [Beer *et al.*, 1994].

1.4.4 Nonlinear Simulation Results

The toroidal gyrofluid equations and bounce averaged trapped electron fluid equations derived in Chapters 2 and 3 are solved via direct numerical simulation using the efficient flux tube geometry in Chapter 4. The most interesting physics results from these simulations are presented in Chapter 5. The importance of small scale, turbulence-generated, sheared poloidal rotation, and the damping of this rotation, is demonstrated. The damping rates of this rotation from magnetic pumping from the gyrofluid model are calculated and compared with neoclassical theory. The nonlinear fluctuation spectra are peaked at long wavelengths compared to the fastest growing linear modes, and are anisotropic in k_r and k_θ, similar to BES measurements [Fonck *et al.*, 1993]. The fluctuation energy balance in the simulations shows that the dominant dissipation mechanism is parallel Landau damping, and that the dominant drive comes from equilibrium density and temperature gradients. Finally, nonlinear simulation results with trapped electrons are presented, where it is found that in moderate or low collisionality regimes, both ion and electron heat transport are strongly dependent on the electron collisionality and electron temperature and density gradients.

1.4.5 Comparison with Experiment

In Chapter 6, results from these nonlinear simulations are compared against a TFTR L-mode discharge, using measured plasma parameters. The predicted transport levels are in reasonable agreement with those calculated from power balance (SNAP). The central transport is small because the linear drive is weak, and increases toward the edge as the linear drive increases. Near $r/a \sim 0.8$, the predicted transport falls off. Possible mechanisms which could increase the predicted transport in the edge are discussed. This behavior is very similar to that found in [Dorland *et al.*, 1994b; Kotschenreuther *et al.*, 1994a], where a transport model based on our toroidal gyrofluid simulations and linear kinetic theory was used to predict temperature profiles. The comparison with experiment is presented here to roughly demonstrate where we stand, and should be considered qualitative. Only one shot is compared here (though [Dorland *et al.*, 1994b; Kotschenreuther *et al.*, 1994a] looked at many shots), and more detailed investigations are necessary.